Soft Matter

PAPER

View Article Online
View Journal | View Issue

Cite this: *Soft Matter*, 2014, **10**, 4458

From multi-ring to spider web and radial spoke: competition between the receding contact line and particle deposition in a drying colloidal drop†

Xin Yang,[a] Christopher Y. Li[b] and Ying Sun*[a]

Received 5th March 2014
Accepted 2nd April 2014

DOI: 10.1039/c4sm00497c

www.rsc.org/softmatter

Deposition morphologies of inkjet-printed colloidal drops are examined under various drying conditions, particle volume fractions, and particle sizes. Concentric multi-rings, radial spokes, spider web, foam, and island-like depositions are observed as a result of the competition between the receding contact line and particle deposition during drop drying. Experimentally measured multi-ring spacing, δR, shows good agreement with the model predicted linear correlation with the local ring radius R. The results also show that the instability near the contact line leads to the radial spoke and saw-toothed structures. The resulting wavelength of the radial structures, λ, satisfies $\lambda \sim \sqrt[3]{R}$ and $\lambda \sim 1/\sqrt[3]{1-\mathrm{RH}}$, where RH is the relative humidity. A dimensionless parameter ξ, defined as the radial deposition growth rate to contact line velocity ratio, has been identified to determine the conditions under which the entire contact line can be pinned to leave a continuous ring deposit. Increasing the particle size while keeping the volume fraction the same is found to suppress the formation of the multi-ring deposition, due to a smaller number of particles available to pin the receding contact line.

1. Introduction

The deposition morphology of colloidal drops containing solution-processed functional nanomaterials is crucial in applications such as inkjet and gravure printing, spray deposition of printable electronics, photovoltaics, and micro-batteries.[1–4] When a colloidal drop with a pinned contact line dries on a substrate, the solvent flow induced by the high evaporation rate at the contact line carries particles to the drop edge, forming the well-known coffee-ring deposit.[5] This evaporatively driven, non-uniform distribution of functional materials in the deposit challenges the quality of printable electronics that often require uniform deposition patterns to achieve better performance. Several approaches have been introduced to suppress the coffee-ring effect by introducing bi-solvents of different surface tensions and vapor pressures to control the Marangoni flow inside the drop[6,7] or by enhancing capillary interactions among asymmetrically-shaped particles (*e.g.*, ellipsoids) on the drop surface.[8]

Contact line depinning can also occur during colloidal droplet evaporation, once the continuously decreasing contact angle reaches its threshold value for receding. The competition between the receding contact line and particle deposition near the contact line results in a variety of deposition patterns, from comb-like structures of stretched DNAs[9] and multi-rings,[10–16] to spider web,[17,18] and spokes.[16,19–21] By moving a meniscus containing colloidal particles at different speeds, Prevo and Velev[22] systematically examined the dependence of deposition morphologies (*e.g.* stripes, uniform layer, foam, and islands) on the contact line velocity in a substrate coating process.

Despite these studies on particle deposition morphologies, quantitative analysis to correlate the characteristic lengths of deposition patterns with droplet drying conditions and colloidal suspension properties is still lacking. With the development of vastly available metallic, semiconductor, and dielectric nanoparticles, nanowires, and polymers as ink materials,[23–25] the challenge now is to effectively assemble these nanoscale building blocks into useful microstructures and devices.[26] Current printing techniques of materials are limited to high-speed production of complex patterns with >10 μm resolution,[27] not compatible with applications that desire nanoscale features.[28] However, by carefully tuning the interplay of wetting, evaporation, and particle self-assembly, the formation of highly repeatable, ordered nanostructures inside inkjet-deposited colloidal drops can potentially be achieved.

In this paper, we report our systematic analysis of the complex morphology transitions inside inkjet-printed evaporating picoliter droplets under different drying conditions, particle volume fractions, and particle sizes. As a result of the competition between contact line receding velocity and particle

[a]*Department of Mechanical Engineering and Mechanics, Drexel University, Philadelphia, PA 19104, USA. E-mail: ysun@coe.drexel.edu; Fax: +1-215-895-1478; Tel: +1-215-895-1373*

[b]*Department of Materials Science and Engineering, Drexel University, Philadelphia, PA 19104, USA*

† Electronic supplementary information (ESI) available. See DOI: 10.1039/c4sm00497c

deposition growth rate, highly repeatable micron and sub-micron deposition structures such as multiple rings, spider web, radial spokes, saw-toothed structures, foams, and islands are observed. A dimensionless parameter that associates the radial deposition growth rate to contact line velocity has been identified to determine whether the entire contact line can be pinned to leave a continuous ring deposit. Both experimental measurement and model prediction of the multi-ring spacing as a function of local ring radius are presented and compared. The wavelengths of the spider web, radial spokes, and saw-toothed deposition structures are quantitatively analyzed using the Marangoni instability theory near the contact line. By varying the particle size while keeping other parameters the same, the effect of particle size on contact line pinning and subsequent deposition pattern is examined.

2. Experimental section

Highly repeatable, pico-liter colloidal drops were generated by a piezoelectric inkjet printhead with an orifice diameter of 60 μm (MicroFab MJ-Al-01) driven by a waveform generator (JetDrive). A high-resolution (0.5 μm per pixel) camera system, consisting of a SensiCam QE CCD camera (Romulus, Michigan), a Navitar 12 Zoom lens (Rochester, New York), and a halogen strobe light (Perkin Elmer), was used to capture side-view images of drop ejection. Details of the experimental setup are described elsewhere.[29]

Colloidal suspensions of sulfate-modified polystyrene beads (Invitrogen) 20 nm and 200 nm in diameters with volume fractions of 0.1%, 0.25% and 0.5% in DI-water were used in the printing experiments. The mixtures of water and particles are homogenized in a sonicator (Cole-Parmer 8891) for 5 minutes before printing.

The relative humidity (RH) levels were controlled at 20%, 40%, and 70% inside the custom-built humidity chamber and the ambient temperature was maintained at 22 °C for all experiments. Glass microscope cover slips (Bellco, ~150 μm thick) were sequentially cleaned by sonicating in Sparkleen-DI water, ethanol and acetone, and then treated by Argon plasma (2 min at 18 W and 250 mTorr, Harrick Plasma PDC-32G). The root-mean-square (RMS) roughness of the plasma-treated glass slides measured by using an atomic force microscope (Digital Instruments/Veeco) is 0.5 nm, much smaller than the particle diameter of 20 and 200 nm. Equilibrium contact angles of the cleaned glass substrates were measured to be close to 0° by using a custom-built goniometer and the LB-ADSA drop analysis plug-in of Image J (http://rsbweb.nih.gov/ij/), where the drop surface is assumed to be a spherical cap and the gravitational effect is neglected (the bond number here is $Bo = \rho g D_0^2/\sigma < 0.005$, where ρ is the drop density, g the gravitational acceleration, D_0 the drop diameter in flight, and σ the drop surface tension).

3. Results and discussion

3.1. Deposition morphology transition in droplets

Fig. 1a–c shows the deposition morphologies of inkjet-printed drops on a cleaned glass substrate at 40% RH with 20 nm particles at volume fractions of 0.5%, 0.25% and 0.1%, respectively. It can be found that the deposition patterns transition from the edge to the center of the drop for all three cases, which are resulted from the competition between the receding contact line and particle deposition at the contact line. Both experimental evidence and models have shown that,[30,31] for a pure liquid drop of spherical-cap shape evaporating on a hydrophilic substrate, the contact line velocity U_{CL} continuously increases with the receding drop radius R. During colloidal drop evaporation, particles inside the drop enhance the stick-slip motion of the contact line, *i.e.*, the contact line radius undergoes a step function that decreases with time. In our study, assuming the particles do not alter the drying properties of the dilute drop of spherical-cap shape, the substrate is very hydrophilic, and the evaporation is diffusion-limited, the velocity of the receding contact line can be approximated as $U_{CL} \sim 1/R(t)$ (see derivation of eqn (A9) in the ESI†), which implies that the contact line velocity gradually increases with the shrinking contact line. Assuming that the particle concentration in the remainder of the evaporating drop keeps constant during drop evaporation, the radial deposition growth rate of particles, U_p, is a constant (see eqn (A10)–(A12) in the ESI†). Here, we introduce a dimensionless parameter, $\xi = U_p/U_{CL}$, to represent the competition between the particle deposition rate and contact line velocity. Fig. 1d shows the linear increase of ξ with drop radius R from

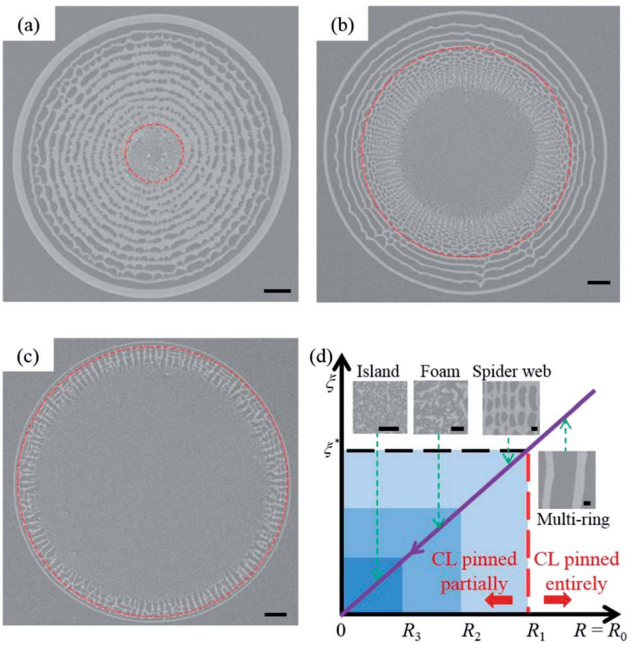

Fig. 1 Scanning electron microscopy images of deposition morphologies inside colloidal drops dried under 40% relative humidity with 20 nm particles at different particle volume fractions: (a) 0.5%, (b) 0.25%, and (c) 0.1%. (d) Deposition morphology transition in (b) as a function of the dimensionless parameter, $\xi = U_p/U_{CL}$, where R_1 corresponds to the evaporating drop radius when $\xi = \xi^*$, the critical value to warrant pinning of the entire contact line. Due to the difficulty in measuring the particle deposition growth rate at a sub-micron scale, ξ *versus* R shown in Fig. 1d is a schematic illustration based on the analysis. The scale bars are 20 μm in (a)–(c) and 2 μm in (d).

the drop center to the edge within a single deposit following $\xi = kR$, using the case of particle volume fraction $\phi = 0.25\%$ (Fig. 1b) as an example. Here, the slope k represents an interplay of the drop contact angle, the particle concentration and diameter, and the porosity and number of layers of the deposition.

As shown in Fig. 1b, for a drop with a particle volume fraction of 0.25%, the initial pinning of the contact line induces the outmost ring-like deposit. As the drop continues to evaporate, the decreasing contact angle at the pinned contact line reaches the critical receding contact angle (a small but finite angle) so that the contact line depins from the outmost ring. At this time, the contact line speed U_{CL} cannot keep up with the particle deposition growth rate U_p, leading to the continuous accumulation of particles at the contact line region until they reach a critical number to pin the contact line again at a distance away from the outmost ring. A new ring is subsequently formed at this newly pinned contact line before another slip motion occurs as the drop evaporates.[19,32–34] The repetitive stick-slip motion of the contact line drives nanoparticles to self-assemble into multi-ring structures for the regime of $R > R_1$ in Fig. 1d and near the drop edge in Fig. 1b, where R_1 corresponds to the radius when $\xi = \xi^*$, the critical value to warrant pinning of the entire contact line. For the case of $\phi = 0.25\%$, $R_1/R_0 = 0.77$, where R_0 is the drop deposition radius. Note that the value of ξ^* is determined by the particle size, volume fraction, and wettability, solvent vapor pressure, relative humidity, and substrate wettability, among others. In this study, we focus on the effects of particle volume fraction, relative humidity and particle size while keeping other parameters unchanged.

As the drop continues to recede, it yields $\xi < \xi^*$ for the regime of $R < R_1$ as shown in Fig. 1d. The contact line velocity keeps increasing but the particle deposition rate is not high enough to pin the entire contact line. This yields only parts of the contact line undergoing the stick-slip motion to form concentric rings, and other parts of the contact line are pinned to produce radial spokes, governed by the instability of the receding drop.[35,36] The combination of stick-slip motion and instability near the contact line leads to the formation of the spider web deposition at $0.77 > R/R_0 > 0.59$. Further receding of the contact line and the increase of U_{CL} yield the deposition morphology transition into interconnected foam structures and finally isolated islands at the drop center where $\xi \ll \xi^*$, as shown in Fig. 1b and d.

Similar deposition morphology transitions are also observed for the particle volume fraction of 0.5%, as shown in Fig. 1a. Due to the decrease of ξ during drop evaporation, the deposition morphology consecutively shows multi-ring, foam and islands from the drop edge to the center where the transition radius $R_1/R_0 = 0.29$. However, for the case of $\phi = 0.1\%$ (Fig. 1c), the deposition morphologies are distinctly different from the ones with higher concentrations. Once the contact line depins from the outmost ring, due to the low particle volume fraction, the particles accumulated at the contact line region do not reach a sufficient number to form multi-ring structures. Instead, the particles accumulate and subsequently deposit periodically at the peaks of the sinusoidal contact line resulting from interfacial instability. The contact line depins locally while leaving periodic regions of the contact line pinned. As the drop evaporates, the magnitude of the finger-like instability grows and the continuously receding contact line pushes the particles to accumulate in the pinned regions and in turn enhances the local pinning of these regions. The radial spoke-like pattern of nanoparticles is hence formed near the edge of the deposit as shown in Fig. 1c. As the contact line continues to recede, the deposition pattern transitions from spokes to foam and islands in the drop center. It is important to note that, the transition radius R_1/R_0 decreases with the particle volume fraction.

3.2. Interfacial instability near the drop contact line

When a droplet recedes on a very hydrophilic substrate, finger-like instability can be observed at the drop contact line,[35] where the thicker parts recede more slowly than the thinner parts leaving behind the radial deposition structures (spokes, spider web, saw-toothed structures) as shown in Fig. 1. For diffusion-limit evaporation of a thin film on a solid substrate, Marangoni instability arises as a result of the evaporation-induced thermal gradients.[36] For the case of an evaporating droplet, the wavelength of the instability follows $\lambda \sim \sqrt[3]{1/Ca} = \sqrt[3]{\sigma R/(\mu j_0)}$, where μ is the liquid viscosity, σ the surface tension, R the drop radius, and j_0 the characteristic evaporation rate.[36] Considering an aqueous drop evaporating on a very hydrophilic substrate with a contact angle $\theta \sim 0^\circ$, the characteristic evaporation rate can be given by $j_0 = 0.65D(1 - \mathrm{RH})c_v/\rho_l$,[35–37] where D is the diffusivity of water vapor in air, RH the relative humidity, c_v the saturated vapor concentration, and ρ_l water density. For the case of constant RH, j_0 is a constant, which follows the scaling law of $\lambda \sim \sqrt[3]{R}$ for Marangoni stress induced instability.

Fig. 2 shows the experimentally measured dimensionless wavelength, λ/R_0, of instability induced radial structures (*i.e.*, spacing of the peaks on saw-toothed structures in multi-ring deposits for $\phi = 0.5\%$ and grid spacing of the spider web shape for $\phi = 0.25\%$) as a function of $\sqrt[3]{R/R_0}$ inside single drops. For both particle volume fractions of 0.25% and 0.5%, the

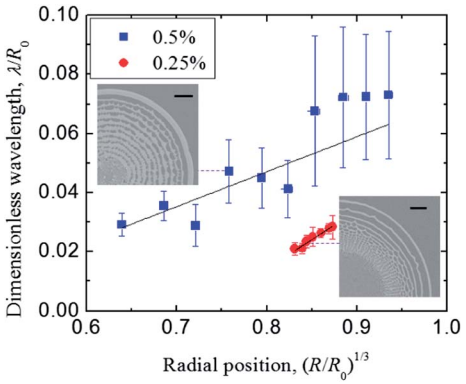

Fig. 2 Wavelength of the saw-toothed structures in multi-ring deposits for $\phi = 0.5\%$ and the grid spacing of spider web for $\phi = 0.25\%$ as a function of $\sqrt[3]{R/R_0}$ resulting from Marangoni instability within single drops containing 20 nm particles and RH = 40%. The scale bars are 20 μm. The error bars are standard deviations from 15 measurements.

wavelength of radial structures increases from the drop center to the edge. Good linear fittings of $\lambda/R_0 \sim \sqrt[3]{R/R_0}$ for both volume fractions of 0.5% and 0.25% in Fig. 2 indicate that instability, resulted from Marangoni stress in diffusion-limited evaporating droplets, is indeed the driving force of particle deposition perpendicular to the contact line. It is important to note that when $0.88 < \sqrt[3]{R/R_0} < 0.90$ for volume fraction of $\phi =$ 0.25%, the deposition pattern transitions from the spider-web shape to the multi-ring structure, where the radial structures vanish. Similar slopes of $\lambda/R_0 \sim \sqrt[3]{R/R_0}$ for particle volume fractions of $\phi = 0.25\%$ and 0.5% are due to the fact that the same viscosity, surface tension, drop size, and substrate wettability are used in both experiments.

Fig. 3 shows the wavelength of radial spokes for colloidal drops dried at relative humidities of 20%, 40% and 70% for $\phi =$ 0.1%. With the increase of humidity from 20% to 70%, the dimensionless wavelength of the spokes, λ/R_0, increases from 0.047 to 0.087. Recall that the Marangoni instability near the contact line yields $\lambda \sim \sqrt[3]{1/Ca} = \sqrt[3]{\sigma R/(\mu j_0)}$ and $j_0 = 0.65D(1 -$ RH$)c_v/\rho_l$.[35–37] A linear correlation relating the wavelength and relative humidity is hence given by $\lambda \sim 1/\sqrt[3]{1 - \mathrm{RH}}$. As shown in Fig. 3, good linearity between the experimentally measured wavelengths of radial spokes λ/R_0 (measured at $R/R_0 = 0.98$) and $1/\sqrt[3]{1 - \mathrm{RH}}$ for relative humidities of 20%, 40% and 70% demonstrate is observed, consistent with the theoretical prediction.

Fig. 4 shows the ring spacing of multi-ring structures, δR, as a function of ring radius, R, for 20 nm particles with particle volume fractions of $\phi = 0.25\%$ and 0.5% evaporated under 40% relative humidity. For both particle volume fractions, the ring spacing increases from the drop center to the edge and the δR *versus* R curves show very good linearity. This linear relationship between ring spacing and drop radius is consistent with the model prediction, $\delta R \sim R$, (see eqn (A16) in the ESI†) that is based on a drop of spherical-cap shape right before and after a small slip motion on a very hydrophilic substrate where evaporation is neglected during slip. As discussed earlier, this stick-slip motion of the contact line is an incremental step of the globally increasing contact line velocity as the drop recedes.

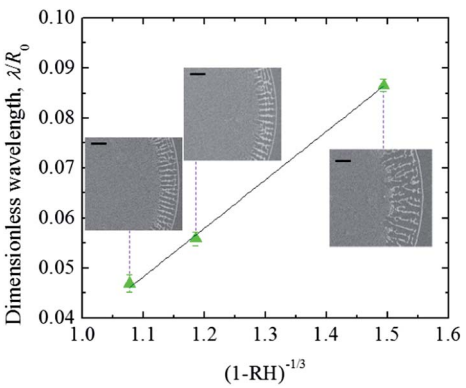

Fig. 3 Wavelength of the radial spokes as a function of $1/\sqrt[3]{1 - \mathrm{RH}}$ for $\phi = 0.1\%$ for drops containing 20 nm particles evaporating at relative humidities of 20%, 40% and 70%. Error bars are standard deviations from 5 measurements. The scale bars are 20 μm.

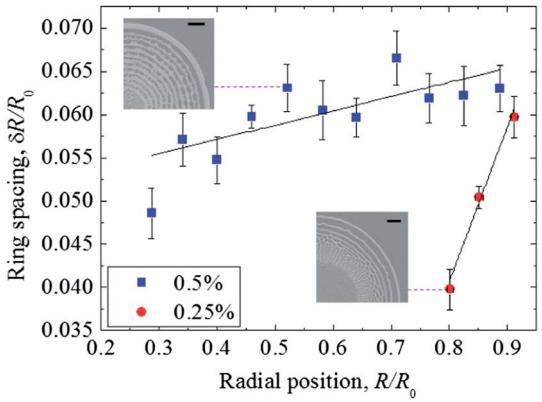

Fig. 4 Ring spacing of multi-ring structures as a function of ring radius for 20 nm particles at volume fractions of 0.25% and 0.5%. The relative humidity is 40%. The outmost ring is not included. Error bars are standard deviations from 8 measurements. The scale bars are 20 μm.

Fig. 4 also shows that, a larger particle volume fraction results in larger ring spacing at the same drop radius, and this is resulted from the enhanced pinning force (accumulation of more particles at the contact line) and depinning energy barrier needed for each ring deposition at a higher particle concentration.[32]

3.3. Effect of particle size

Deposition patterns of colloid drops containing 200 nm particles with volume fractions of 0.5%, 0.25% and 0.1% are shown in Fig. 5a–c, respectively. Similarly to those containing 20 nm particles, ring-like deposits are formed for the cases of $\phi = 0.5\%$ and 0.25% as shown in Fig. 5a and b. As evaporation continues, the depinning forces overwhelm the pinning forces leading to contact line depinning from the outmost ring. In contrast to the repetitive stick-slip motion of the contact line leading to the formation of concentric rings for the cases of 20 nm particles (Fig. 5d), the contact line is only partially pinned for drops containing 200 nm particles resulting in radial spoke structures as shown in Fig. 5a–c. We have shown, by examining the forces acting on particles close to the contact line, that it is the number of particles and not the particle size which dictates particle pining.[29] For drops of the same particle volume fraction but different particle sizes, there are 1000 times more 20 nm particles in a drop than 200 nm particles. As a result, the number of 200 nm particles remaining in the drop after the deposition of the outmost ring is not enough to initiate entire contact line pinning (shown in Fig. 5e). The contact line is only pinned locally to form a series of radial spokes for drops containing 200 nm particles shown in Fig. 5a–c. For the case of $\phi =$ 0.1%, the number of 200 nm particles is so small that even a single ring deposit cannot be formed and the radial spokes break into segments as shown in Fig. 5c.

3.4. Deposition morphology map

The deposition morphology map of multi-ring, spider web, spoke, foam and island structures from inkjet-printed

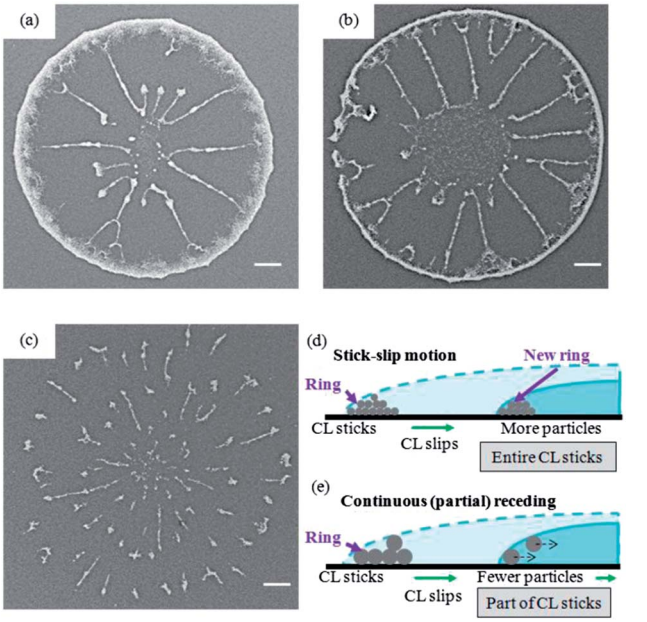

Fig. 5 Scanning electron microscopy images of particle deposition morphologies in colloidal drops containing 200 nm particles at particle loadings of (a) 0.5%, (b) 0.25%, and (c) 0.1%. Schematic illustrations of (d) multi-ring formation in drops containing particles 20 nm in diameter, and (e) radial spokes in drops with particles 200 nm in diameter. Scale bars are 20 μm in (a)–(c).

evaporating colloidal drops as a function of particle concentration and radial position inside the drop is summarized in Fig. 6. Ring deposition occurs in the regime $\xi > \xi^*$ while the contact line is only partially pinned when $\xi < \xi^*$. With the increase in particle loading, the region for ring-like deposition increases, while the region resulting in island-like deposition decreases. For a drop with a given particle loading, as the drop evaporates, the contact line velocity keeps increasing, leading to deposition morphology transitions from the top to the bottom of the morphology map shown in Fig. 6. At a higher particle volume fraction (*e.g.*, $\phi = 0.25\%$ for 20 nm particles) corresponding to a high deposition growth rate, the deposition consequently shows multi-ring, spider web, foam, and islands from the edge to the drop center. However, for a drop with a lower particle volume fraction (*e.g.*, $\phi = 0.1\%$ for 20 nm particles) or a low deposition growth rate, the deposition consequently shows spoke, foam, and islands.

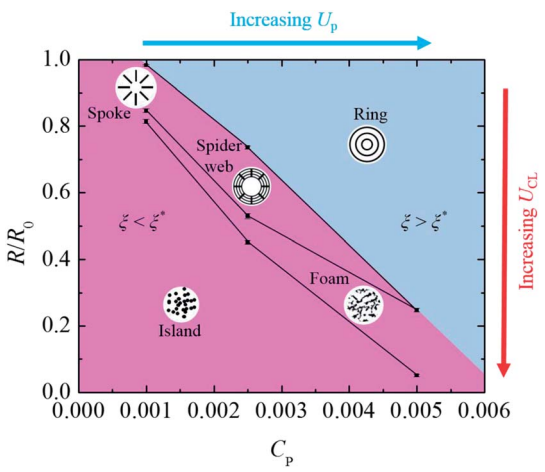

Fig. 6 Deposition morphology map of an inkjet-printed colloidal drop with 20 nm particles, dried under 40% relative humidity showing multi-ring, spoke, spider web, foam and island patterns as a function of the radial position and the particle concentration. Ring deposition occurs for $\xi > \xi^*$ while the contact line is only partially pinned when $\xi < \xi^*$. Error bars are standard deviations from 8 or more measurements.

4. Conclusion

In this paper, we showed that nanoparticles self-assemble into highly repeatable deposition patterns, including concentric multi-ring, radial spokes, spider web, foam, and islands inside inkjet-printed pico-liter colloidal drops. The mechanism governing these deposition morphology transitions in freely evaporating droplets is found to be a result of the competition between the contact line velocity and particle deposition growth rate during drop receding. A variety of particle volume fractions and drying conditions are used to effectively control U_{CL} and U_p, thereby determining the deposition patterns and the critical morphology transition parameter ξ^* to warrant pinning of the entire contact line. Experimental measurements agree well with the model prediction on the linear correlation between multi-ring spacing δR and ring radius R. Marangoni instability near the contact line leads to the radial spoke and saw-toothed structures whose wavelengths λ agree well with the scaling laws of $\lambda \sim \sqrt[3]{R}$ and $\lambda \sim 1/\sqrt[3]{1 - \mathrm{RH}}$. In addition, larger particles are found to suppress the multi-ring deposition as compared to smaller particles.

Besides revealing evaporatively-driven nanoparticle self-assembly mechanisms inside a colloidal drop, this study offers a simple, fast way to produce complex patterns from an inkjet-printed single drop, and hence extends inkjet printing applications to fabricating patterns at sub-micron scales. Future work will focus on the effects of solvent type, as well as the substrate and particle wettability, on the deposition morphology map.

Acknowledgements

We acknowledge the support for this work by the National Science Foundation (grant no. CBET-0968927 and CMMI-1200385).

References

1 F. C. Krebs, S. A. Gevorgyan and J. Alstrup, A roll-to-roll process to flexible polymer solar cells: model studies, manufacture and operational stability studies, *J. Mater. Chem.*, 2009, **19**(30), 5442–5451.
2 E. Tekin, P. J. Smith and U. S. Schubert, Inkjet printing as a deposition and patterning tool for polymers and inorganic particles, *Soft Matter*, 2008, **4**(4), 703–713.

3 M. Pudas, J. Hagberg and S. Leppavuori, Roller-type gravure offset printing of conductive inks for high-resolution printing on ceramic substrates, *Int. J. Electron.*, 2005, **92**(5), 251–269.
4 A. M. Gaikwad, G. L. Whiting, D. A. Steingart and A. C. Arias, Highly Flexible, Printed Alkaline Batteries Based on Mesh-Embedded Electrodes, *Adv. Mater.*, 2011, **23**(29), 3251–3255.
5 R. D. Deegan, O. Bakajin, T. F. Dupont, G. Huber, S. R. Nagel and T. A. Witten, Capillary flow as the cause of ring stains from dried liquid drops, *Nature*, 1997, **389**(6653), 827–829.
6 H. Hu and R. G. Larson, Marangoni effect reverses coffee-ring depositions, *J. Phys. Chem. B*, 2006, **110**(14), 7090–7094.
7 J. Park and J. Moon, Control of colloidal particle deposit patterns within picoliter droplets ejected by ink-jet printing, *Langmuir*, 2006, **22**(8), 3506–3513.
8 P. J. Yunker, T. Still, M. A. Lohr and A. G. Yodh, Suppression of the coffee-ring effect by shape-dependent capillary interactions, *Nature*, 2011, **476**(7360), 308–311.
9 A. Bensimon, A. Simon, A. Chiffaudel, V. Croquette, F. Heslot and D. Bensimon, Alignment and Sensitive Detection of DNA by a Moving Interface, *Science*, 1994, **265**(5181), 2096–2098.
10 L. Shmuylovich, A. Q. Shen and H. A. Stone, Surface morphology of drying latex films: Multiple ring formation, *Langmuir*, 2002, **18**(9), 3441–3445.
11 E. Adachi, A. S. Dimitrov and K. Nagayama, Stripe Patterns Formed on a Glass-Surface during Droplet Evaporation, *Langmuir*, 1995, **11**(4), 1057–1060.
12 S. Maheshwari, L. Zhang, Y. X. Zhu and H. C. Chang, Coupling between precipitation and contact-line dynamics: Multiring stains and stick-slip motion, *Phys. Rev. Lett.*, 2008, **100**(4), 044503.
13 L. Zhang, S. Maheshwari, H. C. Chang and Y. X. Zhu, Evaporative self-assembly from complex DNA-colloid suspensions, *Langmuir*, 2008, **24**(8), 3911–3917.
14 J. Xu, J. F. Xia, S. W. Hong, Z. Q. Lin, F. Qiu and Y. L. Yang, Self-assembly of gradient concentric rings via solvent evaporation from a capillary bridge, *Phys. Rev. Lett.*, 2006, **96**(6), 066104.
15 J. R. Moffat, K. Sefiane and M. E. R. Shanahan, Effect of TiO_2 Nanoparticles on Contact Line Stick-Slip Behavior of Volatile Drops, *J. Phys. Chem. B*, 2009, **113**(26), 8860–8866.
16 W. Han, M. Byun, B. Li, X. C. Pang and Z. Q. Lin, A Simple Route to Hierarchically Assembled Micelles and Inorganic Nanoparticles, *Angew. Chem., Int. Ed.*, 2012, **51**(50), 12588–12592.
17 M. Byun, R. L. Laskowski, M. He, F. Qiu, M. Jeffries-El and Z. Q. Lin, Controlled evaporative self-assembly of hierarchically structured regioregular conjugated polymers, *Soft Matter*, 2009, **5**(8), 1583–1586.
18 S. W. Hong, J. Wang and Z. Q. Lin, Evolution of Ordered Block Copolymer Serpentines into a Macroscopic, Hierarchically Ordered Web, *Angew. Chem., Int. Ed.*, 2009, **48**(44), 8356–8360.
19 R. D. Deegan, O. Bakajin, T. F. Dupont, G. Huber, S. R. Nagel and T. A. Witten, Contact line deposits in an evaporating drop, *Phys. Rev. E: Stat. Phys., Plasmas, Fluids, Relat. Interdiscip. Top.*, 2000, **62**(1), 756–765.
20 B. Li, W. Han, M. Byun, L. Zhu, Q. Z. Zou and Z. Q. Lin, Macroscopic Highly Aligned DNA Nanowires Created by Controlled Evaporative Self-Assembly, *ACS Nano*, 2013, **7**(5), 4326–4333.
21 J. Xu, J. F. Xia and Z. Q. Lin, Evaporation-induced self-assembly of nanoparticles from a sphere-on-flat geometry, *Angew. Chem., Int. Ed.*, 2007, **46**(11), 1860–1863.
22 B. G. Prevo and O. D. Velev, Controlled, rapid deposition of structured coatings from micro- and nanoparticle suspensions, *Langmuir*, 2004, **20**(6), 2099–2107.
23 C. N. Hoth, S. A. Choulis, P. Schilinsky and C. J. Brabec, High photovoltaic performance of inkjet printed polymer: Fullerene blends, *Adv. Mater.*, 2007, **19**(22), 3973–3978.
24 H. H. Lee, K. S. Chou and K. C. Huang, Inkjet printing of nanosized silver colloids, *Nanotechnology*, 2005, **16**(10), 2436–2441.
25 J. A. Rogers and Z. Bao, Printed plastic electronics and paperlike displays, *J. Polym. Sci., Part A: Polym. Chem.*, 2002, **40**(20), 3327–3334.
26 S. C. Glotzer, M. J. Solomon and N. A. Kotov, Self-assembly: From nanoscale to microscale colloids, *AIChE J.*, 2004, **50**(12), 2978–2985.
27 B. Derby, Inkjet Printing of Functional and Structural Materials: Fluid Property Requirements, Feature Stability, and Resolution, *Annu. Rev. Mater. Res.*, 2010, **40**, 395–414.
28 V. M. Shalaev, Optical negative-index metamaterials, *Nat. Photonics*, 2007, **1**(1), 41–48.
29 V. H. Chhasatia and Y. Sun, Interaction of bi-dispersed particles with contact line in an evaporating colloidal drop, *Soft Matter*, 2011, **7**(21), 10135–10143.
30 M. Cachile, O. Benichou, C. Poulard and A. M. Cazabat, Evaporating droplets, *Langmuir*, 2002, **18**(21), 8070–8078.
31 H. Y. Erbil, G. McHale and M. I. Newton, Drop evaporation on solid surfaces: Constant contact angle mode, *Langmuir*, 2002, **18**(7), 2636–2641.
32 D. Orejon, K. Sefiane and M. E. R. Shanahan, Stick-Slip of Evaporating Droplets: Substrate Hydrophobicity and Nanoparticle Concentration, *Langmuir*, 2011, **27**(21), 12834–12843.
33 Y. O. Popov, Evaporative deposition patterns: Spatial dimensions of the deposit, *Phys. Rev. E: Stat., Nonlinear, Soft Matter Phys.*, 2005, **71**(3), 036313.
34 Y. O. Popov and T. A. Witten, Characteristic angles in the wetting of an angular region: Deposit growth, *Phys. Rev. E: Stat., Nonlinear, Soft Matter Phys.*, 2003, **68**(3), 036306.
35 C. Poulard, O. Benichou and A. M. Cazabat, Freely receding evaporating droplets, *Langmuir*, 2003, **19**(21), 8828–8834.
36 E. Sultan, A. Boudaoud and M. Ben Amar, Evaporation of a thin film: diffusion of the vapour and Marangoni instabilities, *J. Fluid Mech.*, 2005, **543**, 183–202.
37 H. Hu and R. G. Larson, Evaporation of a sessile droplet on a substrate, *J. Phys. Chem. B*, 2002, **106**(6), 1334–1344.